Teleoperated Ultrasound Imaging with Confidence Map-based Visual Servoing for Acoustic Coupling Optimization

Hoorieh Mazdarani, and Carlos Rossa
Department of Systems and Computer Engineering, Carleton University, Ottawa, ON, Canada.

***Abstract*—Teleoperated ultrasound (US) imaging is increasingly used in a wide range of clinical applications, enabling remote examination while reducing operator exposure and operator burden. However, acquiring high-quality US images in teleoperated and robotic settings remains challenging, particularly, as the operator must simultaneously maintain acoustic coupling between the probe and the tissue, orient the probe appropriately with respect to the body surface, and compensate for body motion such as respiration or patient movement. These requirements impose a significant cognitive workload and are commonly addressed using force-based control strategies that do not explicitly account for image quality.**

This paper presents a teleoperated robotic US imaging framework that integrates confidence-map–based visual servoing (VS) to autonomously optimize probe-tissue acoustic coupling during imaging. Image features derived from confidence maps are defined to regulate the vertical translation and in-plane orientation of a teleoperated robot-held US probe, ensuring continuous contact and near-normal incidence to the tissue surface subject to motion. This allows the operator to focus exclusively on tissue scanning without the need to manually adjust probe contact or orientation. The proposed approach does not require anatomical models, external tracking systems, or force control as the primary contact regulator, making it well-suited for teleoperated ultrasound imaging across dynamic clinical scenarios. The framework is experimentally validated using realistic lung and kidney mannequins, demonstrating its ability to provide continuous imaging while maintaining optimal acoustic coupling even under respiratory motion.

***Index Terms*—Lung Ultrasound imaging, Teleoperation, Robotic ultrasound imaging, Confidence map, Acoustic coupling**

I. Introduction

Teleoperated ultrasound (US) imaging is increasingly adopted across a wide range of clinical applications, enabling remote examination while reducing operator fatigue [1]–[3]. In many use cases, including lung, breast, liver, and kidney imaging, US provides a radiation-free and real-time alternative to imaging modalities such as computed tomography and radiography [4].

In a teleoperated system, the user operates the robotic agents from a joystick. These systems are designed within three frameworks, i.e., unilateral teleoperation, bilateral teleoperation, and collaborative/shared control. These frameworks differ in the presence or absence of force feedback, and in the degree of autonomy granted to the teleoperated robot [5], [6]. US imaging is one of the most studied uses of such systems [7], [8]. Examples of unilateral teleoperation for ultrasound imaging are provided in [9]–[12]. To partially restore the feeling of interacting with the remote environment, the system designed in [13] provides a mock-up probe and a flexible synthetic platform as the control console; however, it may not perfectly mimic the patient's anatomy.

Shared control is useful in addressing target motion and tissue deformation. In teleoperated US, the robot holding the ultrasound probe can automatically be controlled to ensure appropriate contact with the tissue, while the teleoperator only commands the robot to slide along the tissue's surface. Ensuring proper probe/tissue contact remains a major challenge: insufficient contact force leads to poor acoustic coupling and unclear images, while excessive force can deform the tissue unnecessarily [14]. A dedicated force controller is commonly used to limit the applied force, such as hybrid force/position controllers [15], impedance controllers [16], and admittance controllers [17], [18]. Force sensors are usually expensive and noisy, and the measured force varies with sensor orientation and probe weight, requiring precise online calibration [19], [20]. Furthermore, force control is usually only implemented along the US probe's longitudinal axis [21]–[24], where the controller maintains a constant force but neglects the resulting image quality. In practice, the body surface is uneven, and it is desirable to orient the probe orthogonally to the surface. Several works have addressed this issue by comparing real-time ultrasound images with preoperative images to adjust the contact force [16], [25]. Others, such as Tsumura *et al.* [26], designed actuated end-effectors that acquire diagnostic images with minimal contact force.

In more advanced approaches, an initial path is derived from preoperative images and then adjusted during the procedure. Adjustment methods include trajectory planning with surface perception [27], pose estimation using RGB-D cameras [15], [28]–[30], patient-to-MRI registration [16], [31], and contact posture estimation with optical waveguide force sensors [32]. In parallel, different methods can also adjust the tissue-probe contact force during scanning. Examples include a passive

Email: hooriehmazdarani@cmail.carleton.ca; carlos.rossa@carleton.ca

We acknowledge the support of the Natural Sciences and Engineering Research Council of Canada (NSERC), [funding reference number RGPIN-2025-05468]. Cette recherche a été financée par le Conseil de recherches en sciences naturelles et en génie du Canada (CRSNG), [numéro de référence RGPIN-2025-05468].

spring-based mechanism that pushes the probe against the tissue [33], online optimization to determine the local tissue normal [19], reinforcement learning [34], and task-space compliance control [35].

Rather than relying on force sensors, it is possible to quantify the probe/tissue acoustic coupling from quantitative metrics of the US image itself. Confidence maps, initially proposed in [36], are pixel-wise probability maps showing the reliability of detected features or regions within an image. Chatelain et al. [37] used confidence maps to orient an US probe during teleoperation to achieve optimal image quality and to maintain a target centred in the image in an automated imaging algorithm. With a similar approach, confidence map is also used by Jiang et al. [38] to optimize the in-plane orientation of the probe in an automatic positioning task. However, in both of these works, the contact force is only controlled along the probe's vertical axis, requiring an estimation of the probe's mass, spatial transformations, and the contact stiffness.

In this paper, we propose to integrate confidence maps with visual servoing (VS) to continuously optimize probe–tissue acoustic coupling during teleoperated imaging. The operator uses a haptic device to control the position of a robot arm holding the US probe. As they scan the surface of the tissue, the robot autonomously controls the probe's vertical translation and in-plane rotation to maintain contact and near-normal incidence to the tissue surface, using image features derived from confidence maps. This enables the operator to focus exclusively on imaging intent and anatomical exploration, without the need to manually adjust probe orientation or contact force. Unlike prior approaches that use confidence maps for one-time probe alignment or as supervisory quality indicators, the proposed method incorporates image features derived from confidence maps directly into the controller while imaging a moving tissue surface.

The proposed framework does not require prior knowledge of patient anatomy, external tracking systems, depth cameras, or force control. Instead, acoustic coupling is formulated as an image-quality optimization problem driven solely by real-time ultrasound images. The approach is computationally efficient and well-suited for real-time deployment. The paper is organized as follows. Section 2 introduces the proposed confidence map–based VS algorithm, the image features, and the robot control law with shared autonomy through teleoperation. The experimental setup is presented in Section 3, where the US probe is connected to a robot arm controlled through the teleoperation setup. The feasibility of the proposed method is then demonstrated for 2 different test scenarios in Section 4, followed by a discussion of the obtained results. Finally, in Section 5, a concluding discussion and recommendations for future work are presented.

II. Unified Acoustic Coupling and Teleoperated Imaging

Consider an US probe attached to a robotic arm as in Fig. 1(a). The operator slides the US probe on the tissue surface via a haptic device, while the robot automatically

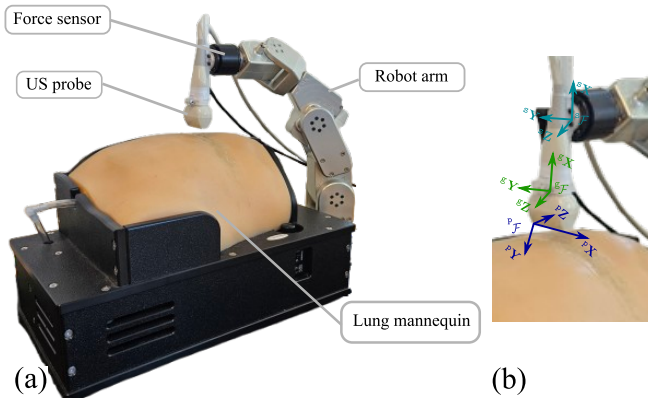

Fig. 1. Robotic US scanning on a lung mannequin in (a) showing the robot arm, the US probe, and the lung mannequin. The mannequin simulates breathing with an internal air pump, which causes the surface to move up and down. In Fig. (b) the force sensor frame ${}^{s}\mathcal{F}$ is defined at the centre of the sensor (the force sensor is not used in the controller), the US probe frame ${}^{p}\mathcal{F}$ placed at the centre of probe's imaging surface, and frame ${}^{g}\mathcal{F}$ defined at the probe's centre of mass.

optimizes the probe-tissue acoustic coupling. Therefore, the objective of the controller is to follow the operator's command in 4-DOF but also to find the velocity of the robot's end effector required to satisfy two complementary objectives: keeping the probe in contact with the body surface ($\mathbf{v}_C$), and following the operator's scanning path commands ($\mathbf{v}_T$). Let the probe velocity vector, as depicted in Fig. 1(b), be:

$$\mathbf{v} = \mathbf{v}_C + \mathbf{v}_T = [v_x \quad v_y \quad v_z \quad \omega_x \quad \omega_y \quad \omega_z]^T, \tag{1}$$

where $\mathbf{v}_T = [v_x \quad 0 \quad v_z \quad \omega_x \quad \omega_y \quad 0]^T$ is a vector of desired velocities received from the haptic device, and $\mathbf{v}_C = [0 \quad v_y \quad 0 \quad 0 \quad 0 \quad \omega_z]^T$ contains the angular and linear probe velocities required to ensure acoustic coupling. The control problem can be formulated by superposition, with $\mathbf{v}_C$ calculated via the VS algorithm [39].

Considering the VS algorithm with the velocity vector $\mathbf{v}'_C \in \mathbb{R}^{2\times 1}$ containing the nonzero elements from $\mathbf{v}_C$ defined in the probe frame ${}^{p}\mathcal{F}$ (see Fig. 1b) and assuming $\mathbf{s} \in \mathbb{R}^{2\times 1}$ to be a vector of measurable and differentiable image features, these two vectors can be related as:

$$\dot{\mathbf{s}} = \mathbf{L}_s \mathbf{v}'_C, \tag{2}$$

where $\mathbf{L}_s \in \mathbb{R}^{2\times 2}$ is the interaction matrix representing the relation between $\mathbf{v}'_C$ and $\dot{\mathbf{s}}$. If the vector of desired features is $\mathbf{s}^*$, the error between the desired and current image features is $\mathbf{e} = \mathbf{s}^* - \mathbf{s}$, and the control action is:

$$\mathbf{v}'_C = \mathbf{K}_p \mathbf{L}_s^{\dagger} \left(\mathbf{s}^* - \mathbf{s}\right), \tag{3}$$

where $\mathbf{K}_p \in \mathbb{R}^{2\times 2}$ is a positive diagonal matrix and $\mathbf{L}_s^{\dagger}$ is the inverse of $\mathbf{L}_s$. This formulation can be shown to decrease the error exponentially, making the features extracted from the real-time images converge to the desired features [40].

Traditionally, the interaction matrix is made up of the partial derivatives of the image features with respect to the camera speed. Here, we used a different approach where $\mathbf{L}_s^{\dagger}$ in (3)

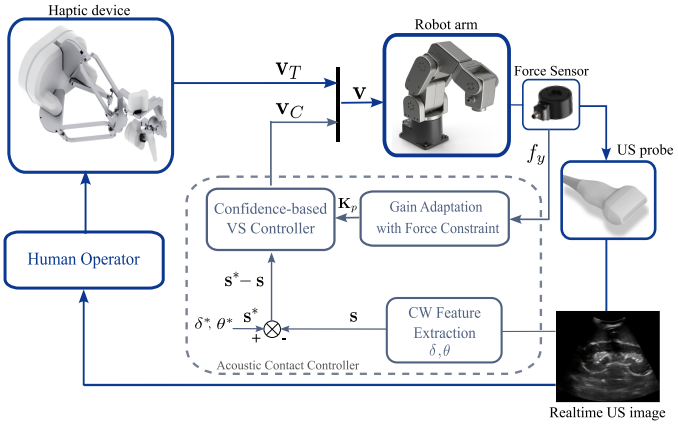

Fig. 2. Block diagram of the proposed algorithm. Real-time US images are used to calculate intensity-weighted (IW) and confidence-weighted (CW) features, which are sent to the VS controller to determine the US probe's speed. The VS control gains are updated according to the current feature values and force constraints.

is arbitrarily chosen among possible generalized forms, such that the probe velocity can be directly written as a function of the image feature error [37]. In this way, it is not necessary to compute the inverse of $\mathbf{L}_s$. Fig. 2 depicts the proposed control approach. The next step is to define appropriate desired image features that are indicative of acoustic coupling between the probe and tissue.

A. Image Features Definition

Image moments of different orders are widely used as image-defining features in computer vision, and their choice is essential to achieve convergence of the controller [41]. We propose to use confidence-weighted image moments, calculated over the confidence map of the US images, to control the probe-tissue contact.

A confidence map is a pixel-based probability map that shows which parts of the image are most reliable, helping assess the quality of the data across different parts of the image. The complete algorithm can be found in [36]. The probability of each pixel in the map depends on the tissue properties and on the path travelled by the acoustic signal. In our application, two main factors can affect the confidence map: The loss of the US signal due to weak or improper acoustic contact, or the existence of a strongly reflective object, such as a rib bone, both of which reduce the confidence level beneath them. These effects can be seen in Fig. 3.

Inspired by [37], we use the barycentre of the confidence map and an associate image feature to orient the probe about ${}^pZ$ (see Fig. 1b), and a second feature to move the probe along ${}^pX$. Confidence map-weighted image moments of order $i+j$ may be derived from the confidence map as:

$$cm_{ij} = \iint_{\mathcal{H}} x^i \; y^j \; \mathbf{C}(x,y) \; dx \; dy, \tag{4}$$

where $\mathbf{C}(x,y) \in [0,1]$ is the confidence of each pixel, and $\mathcal{H}$ is a section of the image. Since these moments are solely

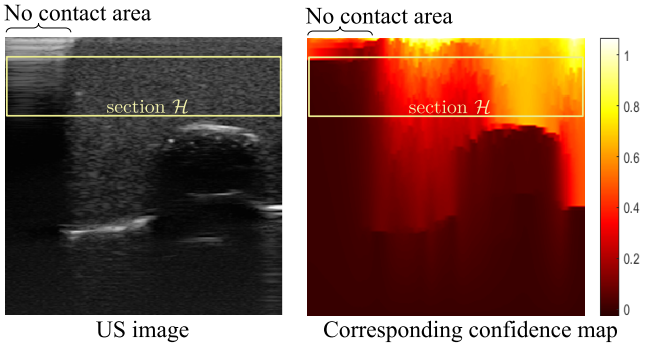

Fig. 3. A sample US image of the a lung phantom (left) when the probe is in partial contact with the tissue and the confidence map (right) showing the effect of improper contact and the rib bone as a highly reflective object. The image section $\mathcal{H}$ is shown. In this image, $\delta = 0.33$, and $\theta = 14°$.

used for contact control, the existence of highly reflective objects in the image should not affect them. Therefore, $\mathcal{H}$ is defined at the top of the image corresponding to the skin layers (see Fig. 3). Two corresponding image features can now be defined. The first feature is the normalized confidence δ in $\mathcal{H}$. It quantifies the contact between the probe and tissue as

$$\delta = (cm_{00})n^{-1}, \tag{5}$$

where n is the total number of pixels in $\mathcal{H}$. When the US probe makes full contact with the tissue $\delta \to 1$, indicating high confidence. As the probe loses contact, $\delta \to 0$ indicates low confidence. Therefore, we can use δ to control the probe vertical displacement by choosing $\mathbf{L}_\delta^\dagger = [-1 \;\; 0]$, as the first row of $\mathbf{L}_s^\dagger$ in (3), and defining the probe velocity along the y axis as:

$$v_y = -k_\delta \; (\delta^* - \delta), \tag{6}$$

where δ^* is the desired δ and $k_\delta > 0$ is a control gain. The second feature gives the orientation of the probe with respect to a vector normal to the tangent of the tissue surface as:

$$\theta = \arctan\left(\frac{cm_{10} - (x_{mid}) \; (cm_{00})}{cm_{01}}\right) \tag{7}$$

where x_{mid} is the horizontal middle point of the image. The angle θ can be employed for controlling the probe's in-plane orientation by choosing the second row of $\mathbf{L}_s^\dagger$ in (3) as $\mathbf{L}_\theta^\dagger = [0 \;\; -1]$, and defining the rotational component of probe velocity about the z axis as:

$$w_z = -k_\theta \; (\theta^* - \theta), \tag{8}$$

where θ^* is the desired θ, and $k_\theta > 0$ is a control gain. If $\theta^* = 0$, the probe is controlled to align with a vector normal to the tissue surface. Since the above is only valid when the probe is in contact with the tissue, δ must be greater than a minimum value and (8) is reformulated with a Sigmoid activation term that depends on δ as:

$$w_z = -k_\theta \; (\theta^* - \theta) \; \frac{1}{1 + e^{\zeta(\delta_{min} - \delta)}}, \tag{9}$$

where δ_{min} is a predefined threshold and $\zeta >> 1$ is a coefficient of the sigmoid function.

Algorithm 1 Teleoperated VS with acoustic coupling

Input: real-time 2D US image
Output: probe velocities $\mathbf{v}$

Initializing:
Set desired features δ^* and θ^*
Set controller parameters: k_δ, k_θ, ζ, δ_{min}, and f_{max}

while probe is teleoperated **do**
  Capture real-time US image
  Calculate confidence map and extract features (5), (7)
  Update variable gain matrix $\mathbf{K}_p$
  Calculate velocity $\mathbf{v}'_C$ (3) and then $\mathbf{v}_C$
  Read teleoperation velocity command $\mathbf{v}_T$
  Calculate probe velocity $\mathbf{v} = \mathbf{v}_C + \mathbf{v}_T$
end while

B. Force Constraint

While the confidence-driven visual servoing algorithm does not require any sensors other than an US probe, in this section add an *optional* constraint to the vertical force f_y the US probe applies to the tissue. The maximum force constraint can be applied by multiplying the control law (6) by a Softplus activation function as:

$$v_y = -k_\delta \ (\delta^* - \delta) \ \log\left[1 + \mathrm{e}^{\zeta(f_{max} - f_y)}\right]. \tag{10}$$

The additional term in the above equation acts as a variable control gain that increases with the difference between the vertical force f_y and maximum allowed force f_{max}. The force $f_\mathtt{y}$ is the second component of the force tensor in the probe frame ${}^\mathtt{p}\mathcal{F}$, that is $f_\mathtt{y} = [0\ 1\ 0\ 0\ 0\ 0]\ {}^\mathtt{p}\mathbf{f}_\mathtt{ext}$, where:

$${}^\mathtt{p}\mathbf{f}_\mathtt{ext} = {}^\mathtt{p}_\mathtt{s}\mathbf{T}\left({}^\mathtt{s}\mathbf{f}_\mathtt{raw} - {}^\mathtt{s}_\mathtt{g}\mathbf{T}\ {}^\mathtt{g}\mathbf{f}_\mathtt{g} - {}^\mathtt{s}\mathbf{f}_\mathtt{offset}\right), \tag{11}$$

and ${}^\mathtt{p}_\mathtt{s}\mathbf{T}$ and ${}^\mathtt{s}_\mathtt{g}\mathbf{T}$ are the force/torque transformation matrices from ${}^\mathtt{s}\mathcal{F}$ to ${}^\mathtt{p}\mathcal{F}$ and from ${}^\mathtt{g}\mathcal{F}$ to ${}^\mathtt{s}\mathcal{F}$, respectively, with the coordinate frames given in Fig. 1(b). For any two coordinate frames a and b, this transformation matrix is defined as:

$${}^\mathtt{b}_\mathtt{a}\mathbf{T} = \begin{bmatrix} {}^\mathtt{b}_\mathtt{a}\mathbf{R} & 0 \\ [{}^\mathtt{b}\mathbf{t}_\mathtt{a}]_\times \ {}^\mathtt{b}_\mathtt{a}\mathbf{R} & {}^\mathtt{b}_\mathtt{a}\mathbf{R} \end{bmatrix} \tag{12}$$

where ${}^\mathtt{b}_\mathtt{a}\mathbf{R}$ and ${}^\mathtt{b}\mathbf{t}_\mathtt{a}$ are the rotation matrix and the translation vector relating two coordinate frames. Here, $[{}^\mathtt{b}\mathbf{t}_\mathtt{a}]_\times$ represents the cross product or the skew-symmetric matrix associated with vector ${}^\mathtt{b}\mathbf{t}_\mathtt{a}$.

The acoustic contact control can be formulated in a VS algorithm, as in (3) where the feature vector is $\mathbf{s} = [\delta \quad \theta]^T$, $\mathbf{L}_s^\dagger$ is a 2×2 negative identity matrix, and $\mathbf{K}_p$ is a diagonal positive definite matrix whose values are:

$$\begin{aligned} k_{1,1} &= k_\delta \log\left[1 + \mathrm{e}^{\zeta(f_{max} - f_y)}\right], \\ k_{2,2} &= k_\theta \left[1 + \mathrm{e}^{\zeta(\delta_{min} - \delta)}\right]^{-1}. \end{aligned} \tag{13}$$

Finally, the probe velocity vector $\mathbf{v}$ is achieved by adding the decoupled vectors $\mathbf{v}_C$ and $\mathbf{v}_T$. The overall algorithm is briefly explained in Algorithm 1.

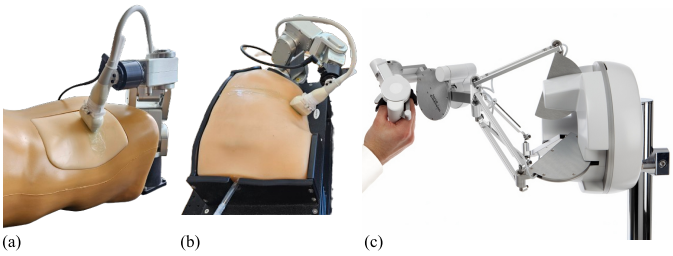

(a) (b) (c)

Fig. 4. Experimental setup in Scenario 1 (a) and 2 (b) using a kidney and a lung mannequin, respectively. (c) The master haptic device used for teleoperated US scanning. The operator scans the desired area using the haptic device, while the robot automatically ensures the proper contact between the probe and the body surface.

III. Experimental Validation and Results

To validate the proposed method we used the setup shown in Fig. 4, where a 40 mm, 7.5 MHz US probe (L15-7H40-A5 from Telemed Ultrasound, Vilnius, Lituania) is attached to the end-effector of a 6-DOF robot arm (Meca500 from Mecademic, Montréal, Canada) through a force/torque sensor (Medusa FT from Bota Systems, Zurich, Switzerland). The US machine streams images at 50 Hz with a depth set to 40 mm. The operator uses a 7 DOF haptic device (Lambda 7 from Force Dimension) to scan the desired tissue area of the lung or kidney phantoms. The algorithm is implemented on an Intel(R) Core i7-9700K computer with a 3.20 GHz CPU and 128 GB of RAM. Matlab is used for US image acquisition and robot control. Both the robot and the haptic device communicate with the computer via EtherCAT/TwinCAT3. Two different test scenarios are implemented using realistic kidney and lung mannequins.

Scenario 1 - Kidney mannequin experiments: In this scenario, see Fig. 4(a), we use a renal biopsy US training mannequin (CAE Blue Phantom, USA) to provide realistic US images and replicate the human anatomy, including ribs, the right kidney with surrounding tissue, and the immediate renal system. We ran 10 trials, during which the operator was scanning the kidney over a 10×10 cm^2 area in 1 minute.

Scenario 2 - Lung mannequin experiments: In this scenario, see Fig. 4(b), we use a lung US training mannequin (CAE Blue Phantom's COVID-19 Lung Simulator) that simulates breathing motion and realistic US images of the left lung with surrounding tissue and ribs. The mannequin simulates breathing with 15 breaths per minute, which is the average for a healthy adult. We ran 10 trials, where the operator scanned the lung over a 20×20 cm^2 area.

Before running the scanning procedure, the US probe is positioned above the tissue surface at a distance of 5-10 cm. As the control procedure begins, the robot automatically moves the probe to make contact with the tissue, after which the operator will start to see US images. In the rest of the trial, the robot follows the operator commands and scans the tissue, while the probe is kept in contact with the tissue. The desired normalized confidence and other controller parameters were

TABLE I
AVERAGE MEDIAN (MED.) AND INTERQUARTILE RANGE (IQR) FOR THE TWO CONTROLLED IMAGE FEATURES AND THE PROBE/TISSUE CONTACT FORCE DURING SCANNING IN ALL TRIALS IN SCENARIOS 1 AND 2.

	δ		θ (deg)		f_y (N)	
Scenario	Med.	IQR	Med.	IQR	Med.	IQR
1	0.43	0.045	-3.50	8.87	2.41	1.05
2	0.41	0.051	-5.60	11.25	2.95	1.66

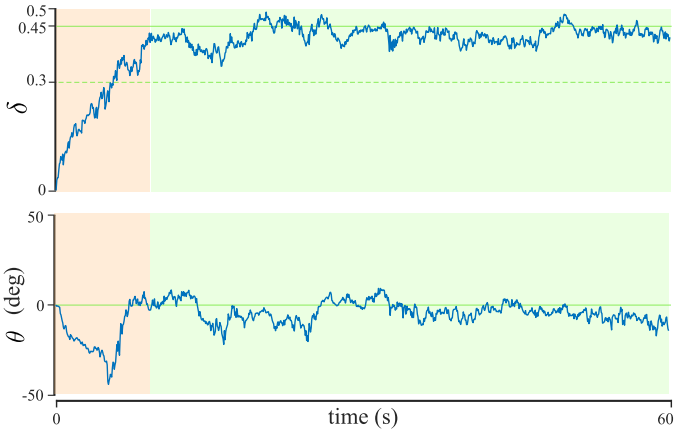

Fig. 5. Results from a trial in Scenario 1. The plots show the measured and desired features δ and θ, calculated from (5) and (7) based on real-time US images. The highlighted areas indicate two phases of the procedure. In the first step (orange), the robot moves the US probe, initially placed away from the body, towards the body surface and adjusts its orientation for full contact until the operator sees a proper US image, after which the operator starts scanning the area while the full contact is ensured automatically (green). The desired features are set to $\delta^* = 0.45$ and $\theta^* = 0$.

selected as follows: $k_\delta = 1.8$, $k_\theta = 0.2$, $\zeta = 100$, $\delta_{min} = 0.30$, $\delta^* = 0.45$, and $f_{max} = 7$ N.

Fig. 5 shows the real-time and the desired image features (i.e., $\delta^* = 0.45$, $\theta^* = 0$) of a representative trial in Scenario 1. As we can see, during the scanning procedure, these features that are controlling the vertical displacement v_y and the rotation w_z of the probe are kept close to the desired values to maintain probe-tissue contact on the uneven surface. Fig. 6 shows the results of a trial in Scenario 2. While in this scenario breathing motion is added, features fluctuate around the desired values still ensure successful probe-tissue contact. Seven US images captured at different time steps during this trial are also shown in Fig. 7 along with the vertical force value applied to the tissue, showing how the controller guaranteed that the force did not exceed the maximum value.

Table I provides a summary of experimental results with the average values of median and interquartile ranges of features and vertical force value in all tests in both scenarios. The applied force in both test scenarios remained bellow the maxixum desired force, while consistent confidence-based features confirm the functionality of the proposed method in automating the acoustic coupling during teleoperated US imaging based only on real-time US images.

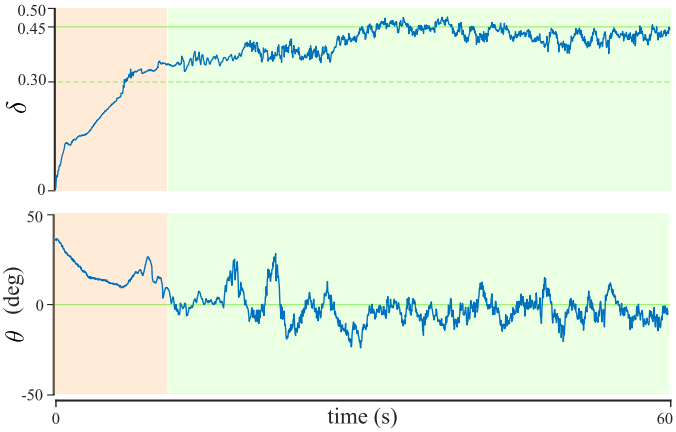

Fig. 6. Results from a representative trial in Scenario 2 with a lung mannequin. The plots show the measured and desired normalized confidence δ and orientation angle θ, calculated from (5) and (7) based on real-time US images. The highlighted areas indicate two phases of the procedure, the same as in Scenario 1. The desired features are set to $\delta^* = 0.45$ and $\theta^* = 0$.

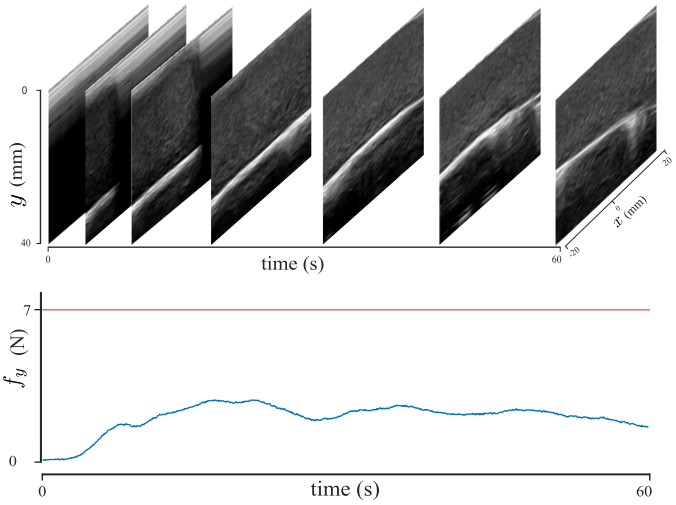

Fig. 7. US images captured at different steps during a trial in Scenario 2 (top) showing the tissue's surface, and the force applied to the tissue (bottom).

IV. CONCLUSION AND FUTURE WORK

In this paper, we developed a confidence map-based VS algorithm designed to ensure proper acoustic contact between the US probe and the tissue surface during teleoperated robotic US imaging subjected to surface motion. The proposed controller follows the operator's motion in 4-DOF used to slide and orient the US probe on the tissue's surface, while automatically controlling other 2-DOF to ensure sufficient acoustic coupling between the tissue and the probe. The controller adjusts the probe's position and orientation in real-time to optimize image quality and may use an optional controller to limit the maximum contact force. The control law determines the US probe's velocity based on features obtained from real-time US images and their corresponding confidence maps, without requiring prior knowledge of the

probe's trajectory or any additional equipment. To the best of our knowledge, this is the first unified confidence map and VS algorithm that 1) ensures probe-tissue contact, 2) optimizes image quality during teleoperated scanning, and 3) operates without additional sensors or trajectory information.

The method was validated experimentally in multiple trials across two distinct scenarios, successfully maintaining proper probe-tissue contact. For such an algorithm to be used in real-time, low complexity and robustness are essential. While previous methods have used depth cameras or force control for surface modelling and contact control, our method relies solely on widely accessible 2D US images with a sampling rate of 50 Hz, which is suitable for real-time implementation without added resources.

REFERENCES

[1] K. Li, Y. Xu, and M. Q.-H. Meng, "An overview of systems and techniques for autonomous robotic ultrasound acquisitions," *IEEE trans. med. robot. bionics*, vol. 3, no. 2, pp. 510–524, 2021.

[2] S. E. Salcudean, H. Moradi *et al.*, "Robot-assisted medical imaging: A review," *Proceedings of the IEEE*, vol. 110, no. 7, pp. 951–967, 2022.

[3] F. Von Haxthausen, S. Böttger *et al.*, "Medical robotics for ultrasound imaging: Current systems and future trends," *Current robotics reports*, vol. 2, no. 1, pp. 55–71, 2021.

[4] Y. Bi, Z. Jiang *et al.*, "Machine learning in robotic ultrasound imaging: Challenges and perspectives," *Annu. Rev. Con. Rob. Auto. Sys.*, vol. 7, no. 1, pp. 335–357, 2024.

[5] Q. Huang, J. Zhou, and Z. Li, "Review of robot-assisted medical ultrasound imaging systems: Technology and clinical applications," *Neurocomputing*, vol. 559, p. 126790, 2023.

[6] W. Si, N. Wang, and C. Yang, "Design and quantitative assessment of teleoperation-based human–robot Collaboration Method for Robot-Assisted Sonography," *IEEE Trans. Autom. Sci. Eng.*, pp. 1–11, 2024.

[7] R. Ye, X. Zhou *et al.*, "Feasibility of a 5g-based robot-assisted remote ultrasound system for cardiopulmonary assessment of patients with coronavirus disease 2019," *Chest*, vol. 159, no. 1, pp. 270–281, 2021.

[8] Z. Jiang, Y. Bi *et al.*, "Intelligent robotic sonographer: Mutual information-based disentangled reward learning from few demonstrations," *Int. J. Robot. Res.*, vol. 43, no. 7, pp. 981–1002, 2024.

[9] C. Delgorge, F. Courrèges *et al.*, "A tele-operated mobile ultrasound scanner using a light-weight robot," *IEEE Trans. Inf. Technol. Biomed.*, vol. 9, no. 1, pp. 50–58, 2005.

[10] J. Zhou, B. Gao, B. Xue, and Q. Huang, "Real-time interaction of a 7-dof robot for teleoperated ultrasonic scanning," in *6th IEEE International Conference on Advanced Robotics and Mechatronics (ICARM)*, 2021, pp. 483–486.

[11] Q. Huang and J. Lan, "Remote control of a robotic prosthesis arm with six-degree-of-freedom for ultrasonic scanning and three-dimensional imaging," *Biomed. Signal Process. Control*, vol. 54, p. 101606, 2019.

[12] B. Duan, L. Xiong, X. Guan, Y. Fu, and Y. Zhang, "Tele-operated robotic ultrasound system for medical diagnosis," *Biomed. Signal Process. Control*, vol. 70, p. 102900, 2021.

[13] "MGIUS-R3 robotic ultrasound system-MGI Tech website-Leading Life Science Innovation." [Online]. Available: https://en.mgi-tech.com/products/instruments_info/11/

[14] Z. Jiang, S. E. Salcudean, and N. Navab, "Robotic ultrasound imaging: State-of-the-art and future perspectives," *Medical Image Analysis*, vol. 89, p. 102878, 2023.

[15] X. Ma, Z. Zhang, and H. Zhang, "Autonomous scanning target localization for robotic lung ultrasound imaging," in *Inter. Conference on Intelligent Robots and Systems*, 2021, pp. 9467–9474.

[16] C. Hennersperger *et al.*, "Towards MRI-based autonomous robotic US acquisitions: a first feasibility study," *Trans Med Imaging*, vol. 36, no. 2, pp. 538–548, 2016.

[17] J. Carriere, J. Fong, T. Meyer, R. Sloboda, S. Husain, N. Usmani, and M. Tavakoli, "An admittance-controlled robotic assistant for semi-autonomous breast ultrasound scanning," in *International symposium on medical robotics (ISMR)*. IEEE, 2019, pp. 1–7.

[18] T.-Y. Fang *et al.*, "Force-assisted ultrasound imaging system through dual force sensing and admittance robot control," *Int J Comput Assist Radiol Surg*, vol. 12, pp. 983–991, 2017.

[19] Z. Jiang *et al.*, "Automatic force-based probe positioning for precise robotic ultrasound acquisition," *Trans Ind Electron*, vol. 68, no. 11, pp. 11 200–11 211, 2020.

[20] J. Jiang *et al.*, "Force tracking control method for robotic ultrasound scanning system under soft uncertain environment," *Actuators*, vol. 13, no. 2, p. 62, 2024.

[21] M. W. Gilbertson and B. W. Anthony, "Force and position control system for freehand ultrasound," *Trans Robot*, vol. 31, no. 4, pp. 835–849, 2015.

[22] R. Finocchi *et al.*, "Co-robotic ultrasound imaging: A cooperative force control approach," in *Medical Imaging: Image-Guided Procedures, Robotic Interventions, and Modeling*, vol. 10135, 2017, pp. 270–280.

[23] T.-Y. Fang *et al.*, "Force-assisted ultrasound imaging system through dual force sensing and admittance robot control," *Int J Comput Assist Radiol Surg*, vol. 12, pp. 983–991, 2017.

[24] H. Mazdarani, B. Sainsbury, J. Watterson, R. Hibbert, and C. Rossa, "Ultrasound-based visual servoing for out-of-plane longitudinal needle tracking in robot-aided percutaneous nephrolithotomy," *IEEE Access*, vol. 13, pp. 69 090–69 102, 2025.

[25] R. Göbl, S. Virga *et al.*, "Acoustic window planning for ultrasound acquisition," *Int J Comput Assist Radiol Surg*, vol. 12, no. 6, pp. 993–1001, 2017.

[26] R. Tsumura, T. Tomioka, Y. Koseki, and K. Yoshinaka, "Safe Contact Force Generation for Robotic Thyroid Ultrasound Imaging," *IEEE Robot. Autom. Lett*, vol. 9, no. 2, pp. 1700–1707, 2024.

[27] J. Tan *et al.*, "Fully automatic dual-probe lung ultrasound scanning robot for screening triage," *Trans Ultrason Ferroelectr Freq Control*, vol. 70, no. 9, pp. 975–988, 2022.

[28] Q. Huang, J. Lan, and X. Li, "Robotic arm based automatic ultrasound scanning for 3D imaging," *Trans Ind Electron*, vol. 15, no. 2, pp. 1173–1182, 2018.

[29] R. Kojcev, A. Khakzar *et al.*, "On the reproducibility of expert-operated and robotic ultrasound acquisitions," *Int J Comput Assist Radiol Surg*, vol. 12, no. 6, pp. 1003–1011, 2017.

[30] J. T. Kaminski, K. Rafatzand, and H. K. Zhang, "Feasibility of robot-assisted ultrasound imaging with force feedback for assessment of thyroid diseases," in *Proceedings of SPIE–the International Society for Optical Engineering*, vol. 11315, 2020, p. 113151D.

[31] S. Virga *et al.*, "Automatic force-compliant robotic ultrasound screening of abdominal aortic aneurysms," in *Inter. Conference on Intelligent Robots and Systems*, 2016, pp. 508–513.

[32] S. Chen *et al.*, "Automatic ultrasound scanning robotic system with optical waveguide-based force measurement," *Int J Comput Assist Radiol Surg*, vol. 16, no. 6, pp. 1015–1025, 2021.

[33] R. Tsumura and H. Iwata, "Robotic fetal ultrasonography platform with a passive scan mechanism," *Int J Comput Assist Radiol Surg*, vol. 15, no. 8, pp. 1323–1333, 2020.

[34] G. Ning, J. Chen, X. Zhang, and H. Liao, "Force-guided autonomous robotic ultrasound scanning control method for soft uncertain environment," *Int J Comput Assist Radiol Surg*, vol. 16, no. 12, pp. 2189–2199, 2021.

[35] J. Wang *et al.*, "Task space compliant control and six-dimensional force regulation toward automated robotic ultrasound imaging," *Trans Autom Sci Eng*, vol. 21, no. 3, pp. 3652–3663, 2023.

[36] A. Karamalis, W. Wein, T. Klein, and N. Navab, "Ultrasound confidence maps using random walks," *Med Image Anal*, vol. 16, no. 6, pp. 1101–1112, 2012.

[37] P. Chatelain, A. Krupa, and N. Navab, "Confidence-driven control of an ultrasound probe," *IEEE Trans Robot*, vol. 33, no. 6, pp. 1410–1424, 2017.

[38] Z. Jiang *et al.*, "Automatic normal positioning of robotic ultrasound probe based only on confidence map optimization and force measurement," *IEEE Robot. Autom. Lett.*, vol. 5, no. 2, pp. 1342–1349, 2020.

[39] S. B. Slotine and B. Siciliano, "A general framework for managing multiple tasks in highly redundant robotic systems," in *proceeding of 5th International Conference on Advanced Robotics*, vol. 2, 1991, pp. 1211–1216.

[40] H. Mazdarani, J. Watterson *et al.*, "Integrating confidence maps and visual servoing for needle tracking in robotic us-guided percutaneous nephrolithotomy," *IEEE Open J. Instrum. Meas.*, vol. 4, pp. 1–9, 2025.

[41] F. Chaumette, "Image moments: a general and useful set of features for visual servoing," *IEEE Trans Robot*, vol. 20, no. 4, pp. 713–723, 2004.